Check for updates

Advanced Materials

ADVANCED MATERIALS
www.advmat.de

RESEARCH ARTICLE OPEN ACCESS

Ultrafast Vertical Organic Electrochemical Transistors With Ion-Permeable Conductive Polymer Top Electrodes

Han-Yan Wu[1] | Yingxue An[1,2] | Luigi Fabiano[1,3] | Qifan Li[1] | Qingqing Wang[4,1] | Feng Zhang[1] | Wenlong Jin[1] | Miao Xiong[1] | Junpeng Ji[1] | Ugo Bruno[1] | Grzegorz Greczynski[5] | Grazia Maria Lucia Messina[3] | Xianjie Liu[1] | Chi-Yuan Yang[1] | Simone Fabiano[1,4,6]

[1]Laboratory of Organic Electronics, Department of Science and Technology, Linköping University, Norrköping, Sweden | [2]Department of Fibre and Polymer Technology, KTH Royal Institute of Technology, Stockholm, Sweden | [3]Laboratory for Molecular Surfaces and Nanotechnology (LAMSUN), Department of Chemical Sciences, University of Catania and CSGI, Catania, Italy | [4]Wallenberg Initiative Materials Science for Sustainability, Department of Science and Technology, Linköping University, Norrköping, Sweden | [5]Thin Film Physics Division, Department of Physics, Chemistry and Biology (IFM), Linköping University, Linköping, Sweden | [6]Wallenberg Wood Science Center, Department of Science and Technology, Linköping University, Norrköping, Sweden

Correspondence: Chi-Yuan Yang (chi-yuan.yang@liu.se) | Simone Fabiano (simone.fabiano@liu.se)

Received: 15 September 2025 | **Revised:** 22 January 2026 | **Accepted:** 29 January 2026

Keywords: BBL | ion-permeable electrodes | PBFDO | vertical OECTs

ABSTRACT

Organic electrochemical transistors (OECTs) combine mixed ionic-electronic transport with bulk electrochemical doping to enable high transconductance and low-voltage operation in aqueous environments, making them attractive for bioelectronics and neuromorphic computing. Vertical OECTs (vOECTs), with channel lengths reduced to tens of nanometers, offer high current densities and compact device footprints, but their performance is fundamentally constrained by ion-impermeable metal top electrodes that restrict ion injection to slow lateral diffusion pathways. Here, we show that electrochemically stable, ion-permeable conductive polymers such as poly(benzodifurandione) (PBFDO) offer a powerful alternative to metal top electrodes in vOECTs. By enabling direct vertical ion injection into poly(benzimidazobenzophenanthroline) (BBL) channels, PBFDO yields devices with high current densities (>400 A cm^{-2}), large on/off ratios (>10^6), and ultrafast switching down to 28 µs, nearly two orders of magnitude faster than equivalent gold-based vOECTs and among the fastest accumulation-mode OECTs reported to date. These results establish a new benchmark for OECT speed and underscore the role of ion-permeable electrodes in overcoming the coupling between electronic and ionic transport in vertical architectures.

1 | Introduction

Organic electrochemical transistors (OECTs) are a distinctive class of devices based on organic mixed ionic-electronic conductors (OMIECs), which offer high transconductance, low-voltage operation, and direct compatibility with aqueous environments [1–3]. These features make them highly attractive for a wide range of applications across sensing, signal processing, and brain-inspired electronics [4–8]. The bulk electrochemical doping of OMIECs enables OECTs to be engineered into vertical device architectures [9–11], thereby reducing the channel length from micrometers to tens of nanometers [12, 13]. Compared to planar devices, such vertical OECTs (vOECTs) drastically reduce device footprints and yield enhanced source-drain current densities [8, 14–19].

Despite these advantages, the performance of vOECTs remains strongly limited by the source/drain electrode configuration [20, 21]. Conventional metallic electrodes like gold, though highly conductive, are inherently impermeable to ions [22]. In vertical

This is an open access article under the terms of the Creative Commons Attribution License, which permits use, distribution and reproduction in any medium, provided the original work is properly cited.

© 2026 The Author(s). *Advanced Materials* published by Wiley-VCH GmbH

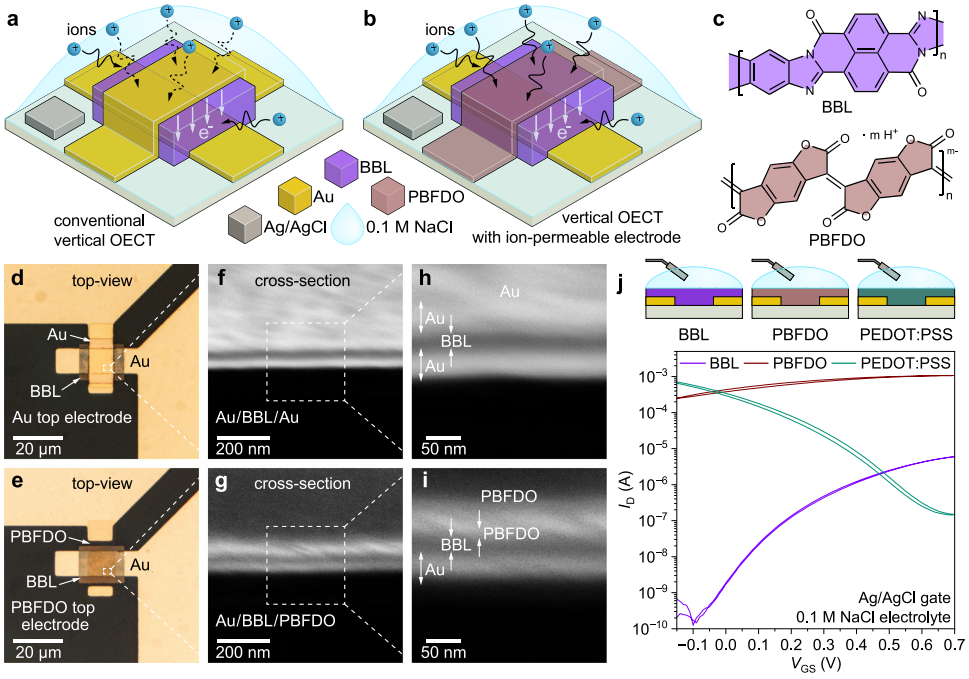

FIGURE 1 | (a,b) Schematics illustrating the ion injection bottleneck in conventional vOECTs with impermeable metal electrodes (a) and efficient ion penetration in vOECTs with permeable polymeric electrodes (b). (c) Chemical structures of the channel semiconductor BBL and the electrode material PBFDO. (d,e) Optical microscope images of vOECTs with Au top electrodes (d) and PBFDO top electrodes (e). (f–i) Cross-section SEM images of vOECTs with Au top electrodes (f,h) and PBFDO top electrodes (g,i). The vOECTs consist of a 50 nm Au bottom electrode, a 20 nm BBL channel, and either a 50 nm Au or a 12 nm PBFDO top electrode. (j) Transfer characteristics of planar OECTs using BBL, PBFDO, and PEDOT:PSS as the channel materials. The planar OECTs have a channel width/length of 50 μm/6 μm; the BBL channel thickness is 20 nm, while the PBFDO and PEDOT:PSS channels are 12 nm thick.

geometries, this restricts ion injection to the electrode edge, forcing ions to travel micrometer-scale lateral distances before fully doping the channel [21]. As a result, gold-based vOECTs typically exhibit transient responses in the millisecond range, falling short of the requirements for applications in bioelectronics and neuromorphic signal processing [11]. Approaches such as introducing pores or cracks into gold top contacts [23–25] or engineering heterojunction channel morphologies [26, 27] can alleviate this bottleneck, but do not overcome the fundamental ion impermeability of dense metals and remain difficult to integrate with standard fabrication. These challenges highlight the need for electrode materials that combine high electrical conductivity with intrinsic ionic permeability.

Here, we demonstrate that permeable and electrochemically stable conductive polymers, such as poly(benzodifurandione) (PBFDO), can serve as effective top electrodes for vOECTs (Figure 1a–c), overcoming the ion injection bottleneck inherent to conventional metal contacts. PBFDO combines remarkable electrical conductivity (>1000 S cm^{-1}) with excellent water and ambient stability, solution processability, and full compatibility with conventional photolithographic patterning [28–36], offering a unique combination of properties not found in traditional metallic or polymeric electrodes. We show that when used as the top electrode in vOECTs with poly(benzimidazobenzophenanthroline) (BBL), a prototypical n-type channel material [37, 38], PBFDO allows ions to permeate directly through the electrode and reach the channel over nanoscale distances, thereby bypassing the lateral ion injection/diffusion bottleneck of metal electrodes. Importantly, PBFDO maintains its high conductivity across the operating voltage window of BBL, with negligible modulation under positive bias. This efficient vertical access accelerates doping dynamics, yielding vOECTs that combine high current density (>400 A cm^{-2}), large on/off ratios (>10^6), and ultrafast transient responses down to 28 μs. This response time is nearly two orders of magnitude faster than that of equivalent BBL-based vOECTs with Au top electrodes under comparable conditions, establishing a new benchmark for OECT switching speed. Together, these results highlight not only the critical role of electrode ion permeability in governing transient dynamics but also the broader interplay between electrode conductivity, ion transport, and electrochemical stability in determining overall device performance.

2 | Results and Discussion

We selected BBL (Figure 1c) as the channel material because of its excellent electron-transport properties and outstanding chemical stability in aqueous electrolytes [39–41]. While BBL enables high-performance operation in lateral OECTs, its implementation in vertical architectures with solid Au electrodes is more challenging. The dense morphology of its side-chain-free backbone hinders lateral ion diffusion, and strategies commonly used to enhance ion transport, such as incorporating hydrophilic binders like Cin-Cell [12], are not compatible due to BBL's solubility in strong acids [37]. For this reason, BBL provides a particularly

15214095, 0, Downloaded from https://advanced.onlinelibrary.wiley.com/doi/10.1002/adma.202518126 by Universita Di Catania, Wiley Online Library on [22/09/2026]. See the Terms and Conditions (https://onlinelibrary.wiley.com/terms-and-conditions) on Wiley Online Library for rules of use; OA articles are governed by the applicable Creative Commons License

stringent and well-defined testbed for exploring the use of top ion-permeable electrodes.

Conventional vOECT with gold top (source) electrodes can be fabricated by first depositing the BBL channel on a glass substrate with pre-patterned bottom gold (drain) electrodes, followed by photolithographic lift-off to define the top evaporated gold electrode (Figure 1d, Figures S1 and S2). A similar approach is used for devices with PBFDO top electrodes (Figure 1e), where the PBFDO is spin-coated, patterned by photolithography, and dry-etched using plasma following the procedure described in the Experimental Section (see also Figures S1 and S2). Cross-sectional scanning electron microscopy (SEM) images show that both gold and PBFDO top contacts form continuous conductive layers (t_{Au} = 50 nm vs. t_{PBFDO} = 12 nm) on top of BBL (t_{BBL} = 20 nm), visible as bright contrasts in Figure 1f–i. This vertical arrangement is further supported by X-ray photoelectron spectroscopy (XPS) depth profiling, which reveals a higher nitrogen content in the bulk region corresponding to BBL (Figure S3). Atomic force microscopy (AFM) measurements confirm that pristine BBL and PBFDO form smooth, compact layers, and that PBFDO spin-coated on top of BBL maintains the same film morphology as the pristine layer (Figure S4). Ultraviolet photoelectron spectroscopy (UPS) measurements show that PBFDO, like gold, exhibits a clear Fermi edge, consistent with the presence of metallic states and in line with its high electrical conductivity (Figure S5). Moreover, BBL's work function (Φ) remains constant whether deposited on gold ($\Phi_{BBL/Au}$ = 4.56 eV) or on PBFDO ($\Phi_{BBL/PBFDO}$ = 4.56 eV), suggesting similar doping behavior at both interfaces (Φ_{Au} = 4.66 eV vs. Φ_{PBFDO} = 4.65 eV).

PBFDO was selected as the top electrode material due to its electrochemical stability within the operating voltage range of BBL and its high electrical conductivity, which remains unchanged under positive gate bias (Figure 1j). When used as the channel in a planar OECT configuration (0.1 M NaCl electrolyte, Ag/AgCl gate electrode), PBFDO exhibits only a modest 2.7× increase in current as V_{GS} is swept from 0 to 0.7 V. This behavior reflects the fact that PBFDO is already in a highly doped state, and further reduction under positive gate bias does not significantly affect its conductivity, in agreement with previous reports [28, 30–32, 35]. In contrast, poly(3,4-ethylenedioxythiophene):polystyrene sulfonate (PEDOT:PSS), undergoes large changes in its redox state under the same conditions, leading to a nearly four-order-of-magnitude drop in conductivity (Figure 1j). Note that BBL-based planar OECTs show several orders of magnitude current modulation over the same voltage range. These results confirm the gate-insensitive behavior of PBFDO and indicate that it can effectively serve as the top electrode in vOECTs, enabling the formation of a narrow vertical channel without limiting the source-drain current.

Next, we investigated whether PBFDO affects the electrochemical doping of BBL by means of spectroelectrochemistry measurements (0.1 M NaCl, Ag/AgCl reference). Upon doping, BBL exhibits strong ground-state bleaching at 300–375 and 450–660 nm, along with pronounced polaron bands at 375–450 and 660–1200 nm (Figure 2a, Figure S6). In contrast, PBFDO shows only a modest reduction in the absorption band above 420 nm and the appearance of a polaron band at 300–420 nm, which we ascribe to further n-doping of PBFDO (Figure 2b, Figure S6). The apparent decrease in absorbance upon electrochemical doping is not due to oxidation of the PBFDO backbone but instead reflects a progressive red-shift of the polaronic absorption, consistent with previous reports [29, 30]. The new features at 300–420 nm are likewise in agreement with the formation of more heavily doped PBFDO species described in these studies. The spectra of the BBL/PBFDO bilayer represent a clear superposition of both components, with distinct BBL polaron absorption (375–450 and 660–920 nm) and bleaching (450–660 nm) visible (Figure 2c, Figure S6). For comparison, a BBL film capped with a thin (30 nm) gold top layer also shows typical BBL-specific features (Figure 2d, Figure S6), but with weaker intensity, likely due to the limited ionic permeability of gold, which restricts vertical ion access and slows electrochemical doping.

The ~400 nm polaron peak of BBL serves as a selective probe, as PBFDO shows negligible signal change in this region. Both pristine BBL and the BBL/PBFDO bilayer exhibit nearly identical voltage-dependent absorption above 0.1 V, increasing steadily to 0.7 V (Figure 2e, Figure S7), indicating that the PBFDO top layer does not impede ion access or charge accumulation. In contrast, BBL/Au shows a delayed onset of polaron formation, with significant signal only appearing above 0.3 V, suggesting that ions must diffuse laterally from the electrode edges due to the gold layer's impermeability. Time-resolved polaron absorption measurements (Figure 2f, Figure S7) confirm that the PBFDO top layer has minimal impact on BBL doping kinetics (τ_{BBL} = 2.23 s vs. $\tau_{BBL/PBFDO}$ = 2.78 s), while the gold top layer significantly delays the process ($\tau_{BBL/Au}$ = 26.5 s).

Electrochemical quartz crystal microbalance with dissipation monitoring (EQCM-D) measurements further support these findings. BBL shows no passive swelling and a gradual active mass uptake above 0.2 V as doping proceeds (Figure 2g), consistent with previous reports [42]. In contrast, PBFDO swells immediately upon contact with the electrolyte, due to its intrinsic doping, and reaches a maximum mass around 0.4 V. The BBL/PBFDO bilayer shows an additive swelling response (Figure 2h), confirming that PBFDO is permeable to ions and allows efficient vertical ion transport into BBL. Note that the slightly lower mass uptake of the BBL/PBFDO bilayer compared to the sum of the individual layers likely arises from partial acoustic decoupling and interfacial ion sharing. Such non-additive behavior is commonly observed in multilayer and composite films, where differences in viscoelastic properties and acoustic impedance between layers influence the effective mass coupling [43, 44].

To further evaluate the impact of the PBFDO top layer on the electrochemical doping of BBL, we conducted electrochemical impedance spectroscopy (EIS) measurements. Pristine BBL shows pronounced capacitive behavior at 0.7 V (Figure 3a, Figures S8 and S9), which can be fitted by a modified Randles circuit (R_s + CPE/R_{ct}, with R_s the active electrolyte resistance, CPE the constant phase element, and R_{ct} the charge transfer resistance). PBFDO exhibits similar capacitive behavior under the same biasing conditions (Figure 3b, Figures S10 and S11). When PBFDO is deposited on BBL, the resulting BBL/PBFDO bilayer retains the characteristic capacitive response of pristine BBL and fits the same equivalent circuit (Figure 3c, Figures S12 and S13), indicating minimal interference from the PBFDO top layer. In contrast, BBL/Au shows markedly different behavior. Its

15214095, 0, Downloaded from https://advanced.onlinelibrary.wiley.com/doi/10.1002/adma.202518126 by Universitá Di Catania, Wiley Online Library on [22/09/2026]. See the Terms and Conditions (https://onlinelibrary.wiley.com/terms-and-conditions) on Wiley Online Library for rules of use; OA articles are governed by the applicable Creative Commons License

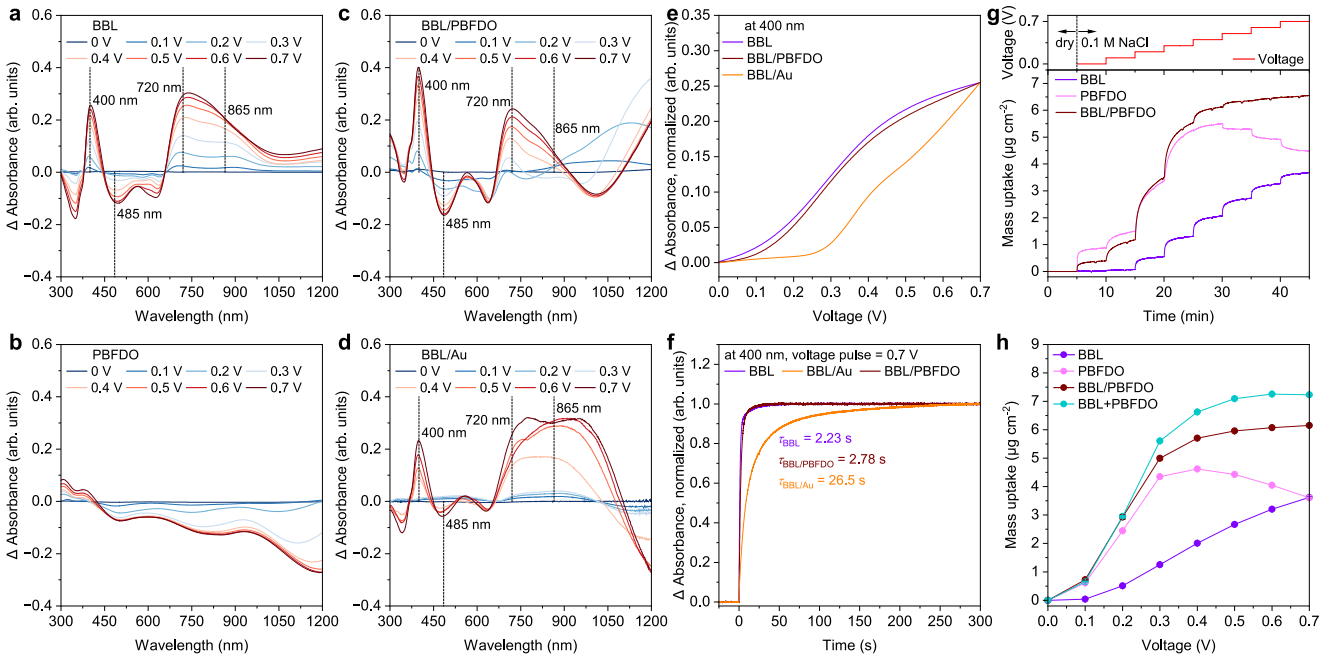

FIGURE 2 | (a–d) Differential absorption spectra of BBL (a), PBFDO (b), BBL/PBFDO (c), and BBL/Au (d) recorded between 0 and 0.7 V versus Ag/AgCl in 0.1 M NaCl aqueous solution. (e) Normalized differential absorption spectra at 400 nm for BBL, BBL/PBFDO, and BBL/Au under the same conditions. (f) Time-resolved normalized differential absorption spectra at 400 nm for BBL, BBL/PBFDO, and BBL/Au during a voltage pulse from 0 to 0.7 V (applied at 0 s). (g) EQCM-D mass uptake of BBL, PBFDO, and BBL/PBFDO between 0 and 0.7 V versus Ag/AgCl in 0.1 M NaCl (seventh overtone). (h) Mass uptake of BBL, PBFDO, BBL/PBFDO, and the calculated sum of BBL and PBFDO (BBL+PBFDO) under different voltages versus Ag/AgCl.

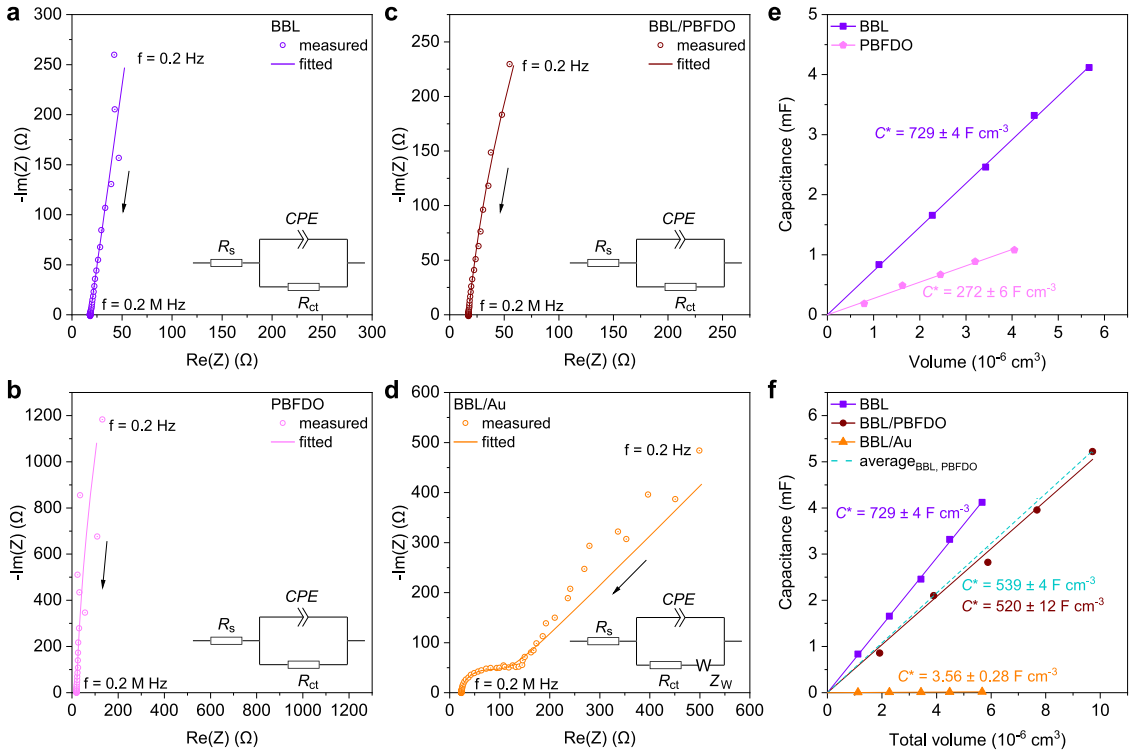

FIGURE 3 | (a–d) Nyquist plots of BBL (a), PBFDO (b), BBL/PBFDO (c), and BBL/Au (d) under 0.7 V bias versus Ag/AgCl electrode in 0.1 M NaCl aqueous solution. Inset: equivalent circuit used for fitting (modified Randles model). (e) Capacitance as a function of polymer volume for BBL or PBFDO under 0.7 V bias. (f) Capacitance as a function of total volume for BBL, BBL/PBFDO, and BBL/Au (volume of Au not counted) under −0.7 V. The thickness-weighted C^* average is shown as a dashed line for comparison.

15214095, 0, Downloaded from https://advanced.onlinelibrary.wiley.com/doi/10.1002/adma.202518126 by Universita Di Catania, Wiley Online Library on [22/09/2026]. See the Terms and Conditions (https://onlinelibrary.wiley.com/terms-and-conditions) on Wiley Online Library for rules of use; OA articles are governed by the applicable Creative Commons License

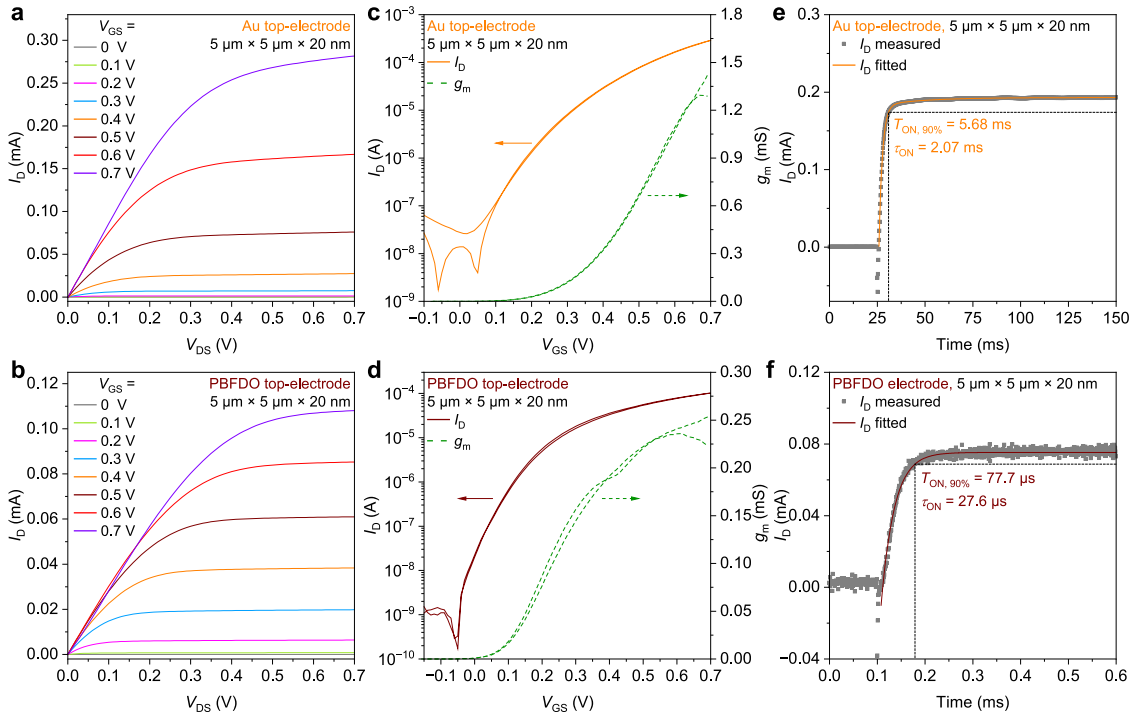

FIGURE 4 | (a,b) Output characteristics, (c, d) transfer characteristics (V_{DS} = 0.7 V), and (e,f) transient response (V_{GS} pulse from 0 to 0.6 V; V_{DS} = 0.6 V) of vOECTs with Au top electrodes (a,c,e) and PBFDO top electrodes (b,d,f). All OECTs have a source/drain overlap area of 5 μm × 5 μm, a 20-nm-thick BBL channel, and either a 50-nm-thick Au or 12-nm-thick PBFDO top electrode. $T_{ON, 90\%}$ is defined as the time interval from the onset of the gate-voltage pulse to the point at which the source-drain current reaches 90% of its saturation value.

EIS spectrum exhibits a 45° slope in the low-frequency region (Figure 3d, Figures S14–S17), indicative of Warburg impedance [45], which arises from limited ion diffusion. This behavior is well described by the modified equivalent circuit $R_s + CPE/(R_{ct} + Z_W)$, suggesting that lateral ion transport from the electrode edges into the BBL bulk is the dominant rate-limiting process. Volumetric capacitance (C^*) analysis further supports this conclusion. Pristine BBL yields a C^* of 729 ± 4 F cm^{-3}, while PBFDO has a C^* of 272 ± 6 F cm^{-3} (Figure 3e). The C^* of the BBL/PBFDO bilayer is 520 ± 12 F cm^{-3} (Figure 3f), which closely matches the thickness-weighted C^* average (539 ± 4 F cm^{-3}). In contrast, BBL/Au exhibits a drastically reduced C^* of only 3.56 ± 0.28 F cm^{-3} (Figure 3e), highlighting the severe restriction of ion access. Together, these results demonstrate that the ion-permeable PBFDO top layer preserves the electrochemical and capacitive responses of BBL, while the dense, impermeable Au layer imposes a strong diffusion barrier (Figure S18).

We then conducted a detailed evaluation of the electrical performance of vOECTs using PBFDO as the top electrode. These devices show output and transfer characteristics comparable to those of Au top-electrode vOECTs, achieving a peak current density of 404 ± 6 A cm^{-2} and an area-normalized transconductance of 966 ± 32 S cm^{-2} (Figure 4a–d, Figures S19–S22). The maximum current and transconductance are approximately three- and sixfold lower, respectively, than in Au-based devices, consistent with the lower conductivity of PBFDO (1.3×10^3 S cm^{-1}) relative to gold (4.1×10^5 S cm^{-1}). While this higher resistance limits current delivery, it can be advantageous for low-current applications such as neuromorphic computing, enabling energy-efficient operation. Overall, the performance remains competitive and well within the range required for high-performance OECT operation (see Table S1). Remarkably, the ~10 nm-thick PBFDO layer combines electronic conductivity with high ionic permeability, enabling direct vertical ion injection into the BBL channel and eliminating the lateral ion-diffusion bottleneck inherent to dense, impermeable metal electrodes such as Au. Consequently, PBFDO top-electrode vOECTs exhibit transient responses up to two orders of magnitude faster than their Au-based counterparts (Figures S20 and S21), reaching τ_{ON} = 28 μs and τ_{OFF} = 8 μs (Figure 4e,f, Figures S22) and ranking among the fastest accumulation-mode OECTs reported to date [8, 12–14, 26]. Moreover, while the response time of Au top-electrode vOECTs scales linearly with source-drain overlap area, reflecting the lateral ion transport limitation, PBFDO top-electrode vOECTs exhibit a weaker area dependence (~area$^{0.6}$), further confirming efficient vertical ion access (Figures S22). This enhanced ion accessibility also leads to a lower threshold voltage ($V_{th} \approx 0.05$ V) compared to Au top-electrode vOECTs ($V_{th} \approx 0.2$–0.3 V; Figure S23). In addition, PBFDO top-electrode vOECTs demonstrate excellent operational stability, retaining 94% of I_D after 10 000 on/off cycles under $V_{GS} = V_{DS} = 0.6$ V (Figure S24).

Finally, we investigated how the thicknesses of the BBL channel and the PBFDO top electrode affect vOECT performance. As the BBL thickness increases, both Au and PBFDO top-electrode devices exhibit reduced maximum source-drain current ($I_{D,max}$) and transconductance ($g_{m,max}$) (Figure 5a,b), along with progressively slower transient responses (Figure 5c,d). In Au top-electrode vOECTs, $I_{D,max}$ and $g_{m,max}$ scale inversely with BBL thickness (Figure 5e), while the response time increases linearly (Figure 5f). In contrast, PBFDO top-electrode vOECTs show a

15214095, 0, Downloaded from https://advanced.onlinelibrary.wiley.com/doi/10.1002/adma.202518126 by Universita Di Catania, Wiley Online Library on [22/09/2026]. See the Terms and Conditions (https://onlinelibrary.wiley.com/terms-and-conditions) on Wiley Online Library for rules of use; OA articles are governed by the applicable Creative Commons License

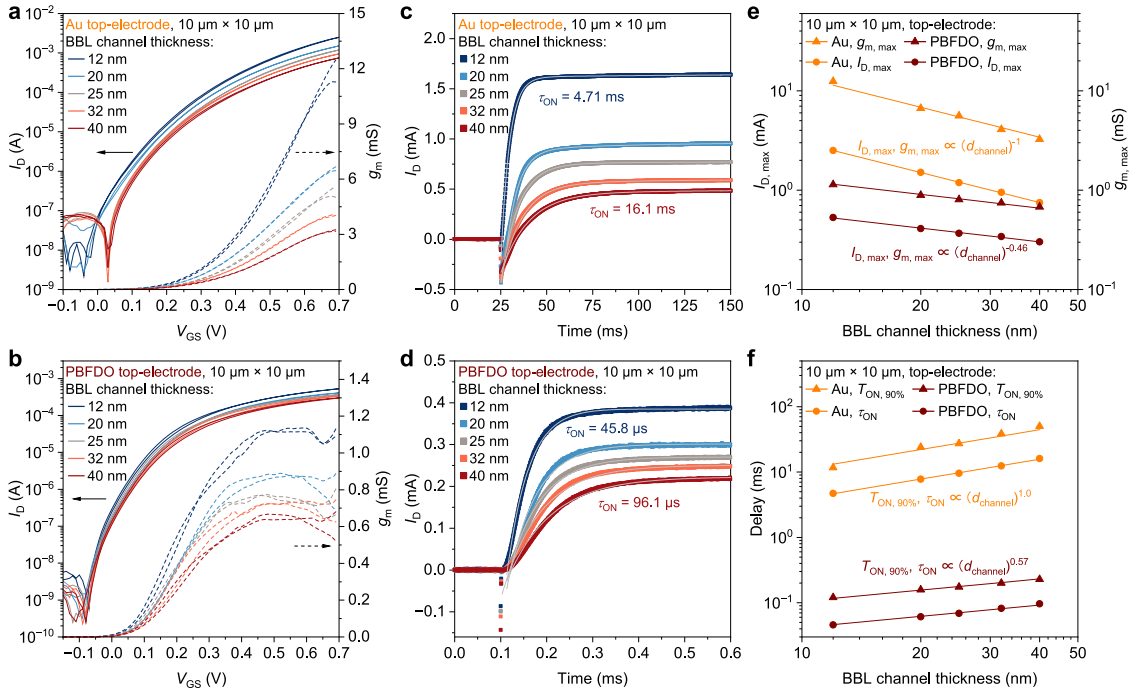

FIGURE 5 | (a,b) Transfer characteristics (V_{DS} = 0.7 V) and (c,d) transient responses (V_{GS} pulse from 0 to 0.6 V; V_{DS} = 0.6 V) of vOECTs with Au top electrodes (a,c) and PBFDO top electrodes (b,d). All devices have a source/drain overlap area of 10 μm × 10 μm, 50-nm-thick Au or 12-nm-thick PBFDO top electrodes, and BBL channel thicknesses ranging from 12 to 40 nm. (e) Channel thickness dependence of maximum drain current and transconductance for vOECTs with Au or PBFDO top electrodes. (f) Channel thickness dependence of rise time parameters for the same devices.

weaker dependence ($I_{D,max}$ and $g_{m,max} \propto d_{BBL}^{-0.5}$ while $T_{ON,90\%}$ and $\tau_{ON} \propto d_{BBL}^{0.6}$). These trends suggest that (1) the high ionic permeability of PBFDO reduces the extent to which ion injection and electrochemical doping limit device speed, and (2) the ~2.7-fold conductivity increase of PBFDO under bias contributes modestly to current enhancement. Varying the PBFDO thickness further supports this interpretation: thicker PBFDO layers yield higher $I_{D,max}$ and $g_{m,max}$ due to lower series resistance but result in slower responses, likely from slightly hindered ion transport and increased capacitance (Figure S25). A PBFDO thickness of ~12 nm offers an optimal trade-off between conductivity and capacitance, maximizing the synergistic performance of the BBL/PBFDO stack (Figure S26). Furthermore, while PBFDO is suitable only for n-type operation due to its instability at negative gate biases, the overall strategy of employing ion-permeable electrodes is general and can be extended to p-type OMIECs. To demonstrate this, we fabricated p-type vOECTs using the glycolated polythiophene P($g_4$2T-T) as the channel and PEDOT:PSS as the top electrode, which is electrochemically stable under p-type conditions. Although not optimized, these devices operated reliably, exhibiting well-defined transfer characteristics and stable performance, confirming the broader applicability of the vertical ion-permeable electrode concept in vOECTs (Figure S27).

3 | Conclusions

In summary, we demonstrated vOECTs with unprecedented performance, achieving transient response times as short as ~28 μs while maintaining high current density (>400 A cm^{-2}) and on/off ratios exceeding 10^6. These results were made possible by integrating an ion-permeable and electrochemically stable PBFDO top electrode, which facilitates efficient vertical ion injection and electrochemical doping of the underlying BBL channel. Spectroelectrochemistry, EQCM-D, and EIS measurements confirm that PBFDO enables ion penetration without compromising volumetric capacitance or doping kinetics, in contrast to conventional dense metal electrodes, such as Au, which restrict ion access. Importantly, this architecture is fully compatible with scalable, solution-based fabrication techniques. By decoupling electronic and ionic transport limitations in vertical geometries, this work provides a design framework for next-generation, ultrafast OECTs with broad relevance for high-speed bioelectronics and neuromorphic systems.

4 | Experimental Section

4.1 | Materials

Naphthalenetetracarboxylic dianhydride (NDA), 1,2,4,5-tetraaminobenzene tetrahydrochloride (TABH), poly(phosphoric acid) (PPA), methanesulfonic acid (MSA), chloroform, 1,2-dichlorobenzene, ethylene glycol, (3-glycidyloxypropyl)trimethoxysilane, 4-dodecylbenzenesulfonic acid, and dimethyl sulfoxide (DMSO) were purchased from Sigma-Aldrich. 3,7-Dihydrobenzo[1,2-b:4,5-b′]difuran-2,6-dione (H-BFDO) was purchased from Tokyo Chemical Industry (TCI). BBL (η = 6.3 dl g^{-1} in MSA at 30°C, M_w = 35 kDa) was synthesized by polycondensation of NDA and TABH in PPA at elevated temperatures, following reported procedures [37, 46]. P($g_4$2T-T) was purchased from 1-Material. Poly(ethylene glycol) diacrylate (PEGDA) was purchased from Sigma-Aldrich. PBFDO was synthesized according to literature methods, yielding a

15214095, 0, Downloaded from https://advanced.onlinelibrary.wiley.com/doi/10.1002/adma.202518126 by Universita Di Catania, Wiley Online Library on [22/09/2026]. See the Terms and Conditions (https://onlinelibrary.wiley.com/terms-and-conditions) on Wiley Online Library for rules of use; OA articles are governed by the applicable Creative Commons License

conductivity of approximately 1300 S cm^{-1} [28, 33]. PEDOT:PSS (Clevios PH1000) was purchased from Heraeus Holding GmbH.

4.2 | Thin-Film Casting

BBL was dissolved in MSA at 50°C for 12 h and then cooled to room temperature to obtain the BBL-MSA solution. The solution was spin-coated onto the OECT substrates (1000 r.p.m., 60 s, acceleration 1000 r.p.m. s^{-1}) to form wet films. Residual MSA was removed by immersing the coated substrates in deionized water, followed by drying under a nitrogen flow [39]. Film thickness was controlled by varying the solution concentration. The PBFDO-DMSO solution was spin-coated onto the OECT substrates at a spin speed of 1000–3000 r.p.m. to obtain half-dry films. These films were subsequently vacuum-dried at 45°C in a vacuum oven to eliminate residual solvent [28, 31]. For PEDOT:PSS, 1 mL of PEDOT:PSS dispersion was diluted with 1 mL of water, followed by the addition of 10 mg of 3-glycidyloxypropyl)trimethoxysilane (GOPS), 50 mg of ethylene glycol, and 1 mg of 4-dodecylbenzenesulfonic acid. The mixture was homogenized in an ultrasonic bath for 30 min, spin-coated at 2000–4000 r.p.m., and annealed at 120°C for 2 min to induce crosslinking and prevent dissolution in water. For P($g_4$2T-T) thin-film fabrication, a mixed solution of PEGDA and P($g_4$2T-T) (6.67 mg mL^{-1} each) was prepared in a chlorobenzene: chloroform (1:2 v/v) solvent mixture. The solution was spin-cast at 1500 r.p.m. for 3 min in an N_2-filled glovebox. The resulting films were crosslinked under 365 nm UV light (Dymax ECE 2000 source) for 5 min, followed by annealing at 100°C for 5 min in a glovebox. The average film thickness was 68 nm.

4.3 | vOECT Fabrication and Characterizations

A schematic of the OECT fabrication process is provided in Figure S1. The OECTs were fabricated on glass substrates. First, a 1.3 µm layer of S1813 photoresist was spin-coated onto the substrate and baked at 115°C for 1 min. The photoresist was then patterned by photolithographic exposure and developed in MF-319 developer. Chromium (5 nm) and gold (50 nm) were deposited by thermal evaporation, followed by lift-off in acetone to define the bottom electrode. Next, a 12–40 nm BBL channel layer was spin-coated. Layers thinner than 12 nm resulted in poor device yield. To pattern the BBL, a 1.3 µm layer of S1813 photoresist was spin-coated, baked (115°C, 1 min), exposed, and developed, followed by reactive ion etching (RIE) to remove excess BBL. The residual photoresist was then removed with acetone, finalizing the BBL channel layer.

For Au top-electrode vOECT, a 1.3 µm S1813 photoresist layer was spin-coated onto the BBL film, baked (115°C, 1 min), exposed, and developed using MF-319 developer. A 50 nm gold layer was deposited by thermal evaporation, and the top electrode was defined by acetone lift-off.

For PBFDO top-electrode vOECT, a 4–40 nm PBFDO layer was spin-coated onto the BBL film. A 1.3 µm S1813 photoresist layer was then applied, baked (115°C, 1 min), exposed, and developed in MF-319 developer. RIE was used to selectively remove unwanted PBFDO. During the RIE process, both the BBL channel and the PBFDO top electrode were protected by a 1.3-µm-thick photoresist layer (Figure S1). The substantial thickness of the photoresist, relative to the underlying BBL and PBFDO films, ensured effective shielding from plasma exposure. The remaining photoresist was subsequently removed with acetone to finalize the top electrode pattern.

For P($g_4$2T-T)-based vOECT with PEDOT:PSS top-electrodes, a P($g_4$2T-T) thin film was spin-coated onto glass substrates with pre-patterned Cr/Au bottom electrodes and photo-crosslinked with PEGDA to prevent dissolution. To define the channel, a 1.3 µm S1813 photoresist layer was spin-coated, baked at 115°C for 1 min, exposed, and developed, followed by RIE to remove excess P($g_4$2T-T). The residual photoresist was then stripped with acetone, completing the channel patterning. Subsequently, a PEDOT:PSS layer was spin-coated onto the patterned P($g_4$2T-T) film and thermally crosslinked using GOPS. A second 1.3 µm S1813 photoresist layer was then applied, baked at 115°C for 1 min, exposed, and developed in MF-319 developer. RIE was used to selectively etch unwanted PEDOT:PSS, and the remaining photoresist was removed with acetone to finalize the top electrode.

Finally, an Ag/AgCl side gate was applied to all vOECTs using Ag/AgCl paste (Sigma-Aldrich, Ag:AgCl = 40:60), and a ~5 µL drop of 0.1 M NaCl was placed in the channel region to complete device fabrication. The source electrode was grounded in all measurements. Electrical characterization was performed using a Keithley 4200A-SCS equipped with a PMU Ultra Fast I–V Module and 4225-RPM Remote Amplifier/Switch Modules.

4.4 | X-Ray Photoelectron Spectroscopy (XPS)

XPS analyses were performed using an Axis Ultra DLD instrument (Kratos Analytical) under a base pressure below 1.1×10^{-9} Torr (1.5×10^{-7} Pa) during spectra acquisition. Monochromatic Al Kα radiation ($h\nu$ = 1486.6 eV) was used with the anode power set to 150 W. All core-level spectra were recorded at normal emission. The analyzer pass energy was set to 20 eV, corresponding to a full width at half maximum of 0.55 eV for the Ag $3d_{5/2}$ peak of a reference Ag foil. Depth profiling was carried out using a 0.5 keV Ar^+ ion beam incident at 20 ° from the surface plane and rastered over an area of 3 × 3 mm^2. The analysis area (0.3 × 0.7 mm^2) was centered within the Ar^+-etching region. Spectrometer calibration was verified by measuring Au $4f_{7/2}$, Ag $3d_{5/2}$, and Cu $2p_{3/2}$ peak positions from sputter-etched Au, Ag, and Cu standards, in accordance with ISO recommendations for monochromatic Al Kα sources [47]. All spectra were charge-referenced to the Au $4f_{7/2}$ line from the substrate [48].

4.5 | Morphology Characterization

SEM images were acquired using a Helios 5 UC FIB-SEM. Cross-sections of the channel were prepared in situ in the SEM chamber using an Ar^+ beam. All cross-sectional images were recorded at a tilt angle of 52°. AFM measurements were performed with a Bruker Dimension Icon XR System.

15214095, 0, Downloaded from https://advanced.onlinelibrary.wiley.com/doi/10.1002/adma.202518126 by Universitá Di Catania, Wiley Online Library on [22/09/2026]. See the Terms and Conditions (https://onlinelibrary.wiley.com/terms-and-conditions) on Wiley Online Library for rules of use; OA articles are governed by the applicable Creative Commons License

4.6 | Ultraviolet Photoelectron Spectroscopy (UPS)

UPS measurements were carried out on a home-built spectrometer equipped with a non-monochromatized He I radiation source ($h\nu = 21.22$ eV). All spectra were acquired at a bias of 3 V under a base pressure below 1×10^{-9} mbar, with binding energies referenced to the Fermi level of Ar^+-sputtered Au. Sample work functions were determined from the secondary electron cutoff.

4.7 | UV-Vis-NIR Absorption Spectra and Spectroelectrochemistry

Absorption spectra were measured in transmission mode. Thick BBL (70 nm) and PBFDO (50 nm) films were prepared to ensure sufficient absorbance. Thin films were deposited by spin-coating onto indium tin oxide (ITO)-coated glass substrates (polymer area ~0.85 cm × 3 cm). BBL, PBFDO, and BBL/PBFDO films were deposited directly onto ITO. For BBL/Au samples, a 30 nm Au layer was thermally evaporated onto BBL films (thicker layers caused strong reflections), and the substrate edges were scraped to expose BBL. Measurements were conducted on a Perkin-Elmer Lambda 900 spectrometer at room temperature. A 0.1 M NaCl aqueous solution served as the electrolyte, the thin films were electrically grounded, and an Ag/AgCl pellet was used as the reference electrode. Voltage biases were applied to the reference electrode using a Keithley 4200A-SCS, sweeping from 0 to 0.7 V in steps of 0.1 V. Before each absorption measurement, the potential was held for 180 s to ensure equilibrium electrochemical doping.

4.8 | Electrochemical Impedance Spectroscopy (EIS)

EIS measurements were performed on glass substrates with patterned Cr/Au electrodes (5/50 nm) in square geometries with side lengths of 4–9 mm (4, 5.7, 7, 8, and 9 mm). Thick BBL (70 nm) and PBFDO (50 nm) films were spin-coated to ensure a high signal-to-noise ratio. For BBL/Au samples, 30 or 50 nm Au was evaporated onto BBL films, and film edges were scraped to expose the polymer. Films outside the electrode area were removed to improve the accuracy of capacitance measurements. Measurements were carried out using a BioLogic SP-200 potentiostat in a 0.1 M NaCl aqueous solution, with a Pt mesh as the counter electrode (CE), a saturated Ag/AgCl electrode as the reference electrode (RE), and the polymer films as the working electrodes (WE). The WE was biased at –0.7 V, and impedance spectra were collected over the frequency range 0.2 Hz-0.2 MHz with an AC amplitude of 10 mV.

4.9 | Electrochemical Quartz Crystal Microbalance (EQCM)

BBL (20 nm) and PBFDO (12 nm) films were spin-coated onto Ti/Au quartz crystals (QSX 338, Biolin Scientific) to prepare BBL, PBFDO, and BBL/PBFDO samples. EQCM measurements were performed on a Q-Sense E4 Analyzer using a degassed 0.1 M NaCl aqueous solution as the electrolyte. The polymer-coated quartz crystals served as the WE, an Ag/AgCl electrode (Dri-Ref-2SH, World Precision Instruments) as the RE, and a Pt electrode as the CE. The WE was biased with a μAutolab potentiostat (Metrohm) from 0 to –0.7 V in steps, holding each bias for 5 min to ensure stabilization. Mass changes were determined using the Sauerbrey equation with QSense Dfind software (Biolin Scientific).

Acknowledgements

This work was financially supported by the Knut and Alice Wallenberg Foundation (2021.0058, 2022.0034, WWSC, and Wallenberg Initiative Materials Science for Sustainability WISE), the Swedish Research Council (2020-03243, 2022–04053, 2022–04553, and 2024–04871), the European Research Council through the ERC Consolidator Grant project INFER (101125879), the European Commission through the FET-OPEN project MITICS (964677), the Pathfinder OPEN project ICONIC (101129638), and the MSCA-IF-2020 project PSOECNs (101151352), the Swedish Foundation for Strategic Research (IS24-0162), and the Swedish Government Strategic Research Area in Materials Science on Functional Materials at Linköping University (Faculty Grant SFO-Mat-LiU 2009-00971).

Conflicts of Interest

The authors declare no conflicts of interest.

Data Availability Statement

The data that support the findings of this study are available from the corresponding author upon reasonable request.

References

1. J. Rivnay, S. Inal, A. Salleo, R. M. Owens, M. Berggren, and G. G. Malliaras, "Organic Electrochemical Transistors," *Nature Reviews Materials* 3 (2018): 17086, https://doi.org/10.1038/natrevmats.2017.86.

2. B. D. Paulsen, K. Tybrandt, E. Stavrinidou, and J. Rivnay, "Organic Mixed Ionic–Electronic Conductors," *Nature Materials* 19 (2019): 13–26, https://doi.org/10.1038/s41563-019-0435-z.

3. P. Gkoupidenis, Y. Zhang, H. Kleemann, et al., "Organic Mixed Conductors for Bioinspired Electronics," *Nature Reviews Materials* 9 (2023): 134–149, https://doi.org/10.1038/s41578-023-00622-5.

4. Z. Jiang, D. Ye, L. Xiang, et al., "A Drug-Mediated Organic Electrochemical Transistor for Robustly Reusable Biosensors," *Nature Materials* 23 (2024): 1547–1555, https://doi.org/10.1038/s41563-024-01970-5.

5. A. Marks, S. Griggs, N. Gasparini, and M. Moser, "Organic Electrochemical Transistors: An Emerging Technology for Biosensing," *Advanced Materials Interfaces* 9 (2022): 2102039, https://doi.org/10.1002/admi.202102039.

6. S. Wang, X. Chen, C. Zhao, et al., "An organic Electrochemical Transistor for Multi-Modal Sensing, Memory And Processing," *Nature Electronics* 6 (2023): 281–291, https://doi.org/10.1038/s41928-023-00950-y.

7. P. C. Harikesh, D. Tu, and S. Fabiano, "Organic Electrochemical Neurons for Neuromorphic Perception," *Nature Electronics* 7 (2024): 525–536, https://doi.org/10.1038/s41928-024-01200-5.

8. Y. Yao, R. M. Pankow, W. Huang, et al., "An Organic Electrochemical Neuron For A Neuromorphic Perception System," *Proceedings of the National Academy of Sciences* 122 (2025): 2414879122, https://doi.org/10.1073/pnas.2414879122.

9. M. J. Donahue, A. Williamson, X. Strakosas, et al., "High-Performance Vertical Organic Electrochemical Transistors," *Advanced Materials* 30 (2018): 1705031, https://doi.org/10.1002/adma.201705031.

10. R. B. Rashid, W. Du, S. Griggs, I. P. Maria, I. McCulloch, and J. Rivnay, "Ambipolar Inverters Based On Cofacial Vertical Organic

15214095, 0, Downloaded from https://advanced.onlinelibrary.wiley.com/doi/10.1002/adma.202518126 by Universita Di Catania, Wiley Online Library on [22/09/2026]. See the Terms and Conditions (https://onlinelibrary.wiley.com/terms-and-conditions) on Wiley Online Library for rules of use; OA articles are governed by the applicable Creative Commons License

Electrochemical Transistor Pairs For Biosignal Amplification," *Science Advances* 7 (2021): abh1055.

11. C. Cea, Z. Zhao, D. J. Wisniewski, et al., "Integrated Internal Ion-Gated Organic Electrochemical Transistors For Stand-Alone Conformable Bioelectronics," *Nature Materials* 22 (2023): 1227–1235, https://doi.org/10.1038/s41563-023-01599-w.

12. W. Huang, J. Chen, Y. Yao, et al., "Vertical Organic Electrochemical Transistors For Complementary Circuits," *Nature* 613 (2023): 496–502, https://doi.org/10.1038/s41586-022-05592-2.

13. J. Kim, R. M. Pankow, Y. Cho, et al., "Monolithically Integrated High-Density Vertical Organic Electrochemical Transistor Arrays And Complementary Circuits," *Nature Electronics* 7 (2024): 234–243, https://doi.org/10.1038/s41928-024-01127-x.

14. L. Gao, Q. Zhang, Y. Lai, et al., "High-Loading Homogeneous Crosslinking Enabled Ultra-Stable Vertical Organic Electrochemical Transistors For Implantable Neural Interfaces," *Nano Energy* 129 (2024): 110062, https://doi.org/10.1016/j.nanoen.2024.110062.

15. S. Cong, J. Chen, M. Xie, et al., "Single Ambipolar OECT–Based Inverter With Volatility and Nonvolatility on Demand," *Science Advances* 10 (2024): adq9405, https://doi.org/10.1126/sciadv.adq9405.

16. Z. Deng, Y. Yu, Y. Zhou, et al., "Ternary Logic Circuit and Neural Network Integration via Small Molecule-Based Antiambipolar Vertical Electrochemical Transistor," *Advanced Materials* 36 (2024): 2405115, https://doi.org/10.1002/adma.202405115.

17. Y. Lai, J. Cheng, M. Xie, et al., "Precisely Patterned Channels in a Vertical Organic Electrochemical Transistor With a Diazirine Photo-Crosslinker," *Angewandte Chemie International Edition* 63 (2024): 202401773, https://doi.org/10.1002/anie.202401773.

18. Y. Sun, Y. Lan, M. Li, et al., "Indacenodithiophene-Based Single-Component Ambipolar Polymer For High-Performance Vertical Organic Electrochemical Transistors and Inverters," *Aggregate* 5 (2024): 577.

19. Y. Cho, L. Gao, Y. Yao, et al., "Small-Molecule Mixed Ionic-Electronic Conductors for Efficient N-Type Electrochemical Transistors: Structure-Function Correlations," *Angewandte Chemie International Edition* 64 (2025): 202414180, https://doi.org/10.1002/anie.202414180.

20. S. Hou, W. Zuo, Q. Fang, et al., "Modulation on Transconductance and Switching Speed of Vertical Organic Electrochemical Transistors via Structure Engineering," *ACS Applied Materials & Interfaces* 17 (2025): 5176–5183, https://doi.org/10.1021/acsami.4c17931.

21. R. Wu, C. Wu, J. Zhou, et al., "Effect of Channel Patterning Precision On The Performances Of Vertical OECTs," *Nanoscale* 17 (2025): 8634–8641, https://doi.org/10.1039/D4NR05239K.

22. T. Li, Z. Qu, J. Si, Y. Lee, V. K. Bandari, and O. G. Schmidt, "Monolithically Integrated Solid-State Vertical Organic Electrochemical Transistors Switching Between Neuromorphic And Logic Functions," *Science Advances* 11 (2025): adt5186.

23. C. Zhang, L. Margotti, F. Decataldo, et al., "Organic Mixed Ionic Electronic Conductor Nanochannels for Vertical Electrochemical and Ionic Transistors," *Advanced Electronic Materials* 10 (2024): 2300762, https://doi.org/10.1002/aelm.202300762.

24. Y. Zhong, Q. Liang, Z. Chen, et al., "High-Performance Fiber-Shaped Vertical Organic Electrochemical Transistors Patterned by Surface Photolithography," *Chemistry of Materials* 35 (2023): 9739–9746, https://doi.org/10.1021/acs.chemmater.3c02237.

25. S. Dai, X. Zhang, X. Liu, et al., "Vertical-Structure Overcomes the Strain Limit of Stretchable Organic Electrochemical Transistors," *Advanced Materials* 37 (2025): 2413951, https://doi.org/10.1002/adma.202413951.

26. S. Wang, Y. Wang, X. Cai, et al., "A High-Frequency Artificial Nerve Based On Homogeneously Integrated Organic Electrochemical Transistors," *Nature Electronics* 8 (2025): 254–266, https://doi.org/10.1038/s41928-025-01357-7.

27. S. Wang, M. Wang, S. Zhang, et al., "Fullerene-Derivative-Induced Hilly Morphology For High-Speed Flexible Organic Electrochemical Transistors," *Materials Horizons* 12 (2025): 10170–10183, https://doi.org/10.1039/d5mh01028d.

28. H. Tang, Y. Liang, C. Liu, et al., "A Solution-Processed n-Type Conducting Polymer With Ultrahigh Conductivity," *Nature* 611 (2022): 271–277, https://doi.org/10.1038/s41586-022-05295-8.

29. Z. Ke, A. Abtahi, J. Hwang, et al., "Highly Conductive and Solution-Processable n-Doped Transparent Organic Conductor," *Journal of the American Chemical Society* 145 (2023): 3706–3715, https://doi.org/10.1021/jacs.2c13051.

30. Y. Liang, C. Che, H. Tang, et al., "Influence of Interaction Between Electrolyte With Side-Chain Free Conjugated Polymer On The Performance Of Organic Electrochemical Transistors," *ACS Applied Materials & Interfaces* 16 (2023): 19977.

31. H. Tang, Y. Liang, C.-Y. Yang, et al., "Polyethylene Glycol-Decorated n-Type Conducting Polymers With Improved Ion Accessibility For High-Performance Organic Electrochemical Transistors," *Materials Horizons* 11 (2024): 5419–5428, https://doi.org/10.1039/D4MH00979G.

32. X. Wu, H. Tang, Z. Zhou, et al., "Improved Stability and Performance of an n-Type Depletion Mode Poly(benzodifurandione) Based Organic Electrochemical Transistor via Electrolyte Selection," *Chemistry of Materials* 36 (2024): 8639–8648.

33. J. D. Huang, Q. Li, Q. Wang, et al., "Preventing Benzoquinone-Based Catalyst Aggregation Enables the One-Step Synthesis of Highly Conductive Poly(benzodifurandione) Without Post-Reaction Purification," *Advanced Materials* 37 (2025): 2502426, https://doi.org/10.1002/adma.202502426.

34. J. H. Kim, I. Lee, W.-J. Lee, et al., "Sterilizable Vertical n-Type Organic Electrochemical Transistors For Skin-Conformal ECG Monitoring," *Materials Science and Engineering: R: Reports* 165 (2025): 101003, https://doi.org/10.1016/j.mser.2025.101003.

35. H. Tang, Z. Xu, Y. Liang, et al., "Highly Conductive Alcohol-Processable n-Type Conducting Polymer Enabled by Finely Tuned Electrostatic Interactions for Green Organic Electronics," *Angewandte Chemie, International Edition* 64 (2025): 202415349.

36. J. Zhang, Y. Zhong, H. Jiang, et al., "Trace Dual-Crosslinkable Additives Enable Direct Microlithography for Enhanced Organic Electrochemical Transistors," *Advanced Materials* 37 (2025): 2417452, https://doi.org/10.1002/adma.202417452.

37. H. Y. Wu, C. Y. Yang, Q. Li, et al., "Influence of Molecular Weight on the Organic Electrochemical Transistor Performance of Ladder-Type Conjugated Polymers," *Advanced Materials* 34 (2022): 2106235, https://doi.org/10.1002/adma.202106235.

38. H. Sun, M. Vagin, S. Wang, et al., "Complementary Logic Circuits Based on High-Performance n-Type Organic Electrochemical Transistors," *Advanced Materials* 30 (2018): 1704916, https://doi.org/10.1002/adma.201704916.

39. P. C. Harikesh, C. Y. Yang, H. Y. Wu, et al., "Ion-Tunable Antiambipolarity In Mixed Ion–Electron Conducting Polymers Enables Biorealistic Organic Electrochemical Neurons," *Nature Materials* 22 (2023): 242–248, https://doi.org/10.1038/s41563-022-01450-8.

40. P. C. Harikesh, C. Y. Yang, D. Tu, et al., "Organic Electrochemical Neurons And Synapses With Ion Mediated Spiking," *Nature Communications* 13 (2022): 901, https://doi.org/10.1038/s41467-022-28483-6.

41. J. Ji, D. Gao, H. Y. Wu, et al., "Single-Transistor Organic Electrochemical Neurons," *Nature Communications* 16 (2025): 4334, https://doi.org/10.1038/s41467-025-59587-4.

42. J. Surgailis, A. Savva, V. Druet, et al., "Mixed Conduction in an N-Type Organic Semiconductor in the Absence of Hydrophilic Side-Chains," *Advanced Functional Materials* 31 (2021): 2010165, https://doi.org/10.1002/adfm.202010165.

15214095, 0, Downloaded from https://advanced.onlinelibrary.wiley.com/doi/10.1002/adma.202518126 by Universita Di Catania, Wiley Online Library on [22/09/2026]. See the Terms and Conditions (https://onlinelibrary.wiley.com/terms-and-conditions) on Wiley Online Library for rules of use; OA articles are governed by the applicable Creative Commons License

43. V. Dargel, N. Shpigel, S. Sigalov, et al., "In Situ Real-Time Gravimetric And Viscoelastic Probing Of Surface Films Formation On Lithium Batteries Electrodes," *Nature Communications* 8 (2017): 1389, https://doi.org/10.1038/s41467-017-01722-x.

44. I. Reviakine, D. Johannsmann, and R. P. Richter, "Hearing What You Cannot See and Visualizing What You Hear: Interpreting Quartz Crystal Microbalance Data From Solvated Interfaces," *Analytical Chemistry* 83 (2011): 8838–8848, https://doi.org/10.1021/ac201778h.

45. J. Huang, "Diffusion Impedance Of Electroactive Materials, Electrolytic Solutions And Porous Electrodes: Warburg Impedance and Beyond," *Electrochimica Acta* 281 (2018): 170–188, https://doi.org/10.1016/j.electacta.2018.05.136.

46. F. E. Arnold and R. Van Deusen, "Preparation and Properties of High Molecular Weight, Soluble Oxobenz[de]imidazobenzimidazoisoquinoline Ladder Polymer," *Macromolecules* 2 (1969): 497–502, https://doi.org/10.1021/ma60011a009.

47. ISO15472:2010, ISO, Geneva 2010.

48. G. Greczynski and L. Hultman, "Binding Energy Referencing in X-Ray Photoelectron Spectroscopy," *Nature Reviews Materials* 10 (2025): 62–78, https://doi.org/10.1038/s41578-024-00743-5.

Supporting Information

Additional supporting information can be found online in the Supporting Information section.

Supporting File: adma72415-sup-0001-SuppMat.pdf.

15214095, 0, Downloaded from https://advanced.onlinelibrary.wiley.com/doi/10.1002/adma.202518126 by Università Di Catania, Wiley Online Library on [22/09/2026]. See the Terms and Conditions (https://onlinelibrary.wiley.com/terms-and-conditions) on Wiley Online Library for rules of use; OA articles are governed by the applicable Creative Commons License